Article

Facile Preparation of Fe_3O_4 Nanoparticles/Reduced Graphene Oxide Composite as an Efficient Anode Material for Lithium-Ion Batteries

Muhammad Usman Hameed [1,*], **Muhammad Yasir Akram** [2,*], **Ghulam Ali** [3] ID, **Muhammad Hafeez** [4], **Faizah Altaf** [1,*], **Ashfaq Ahmed** [1], **Shabnam Shahida** [5] **and Patrizia Bocchetta** [6] ID

1   Department of Chemistry, Women University of Azad Jammu & Kashmir, Bagh 12500, Pakistan;
    ashfaqahmad1546@gmail.com
2   Department of Chemistry and Humanities, Khawaja Fareed University of Engineering and Information
    Technology, Rahim Yar Khan 64200, Pakistan
3   USPCAS-E, National University of Sciences and Technology (NUST), Islamabad 44000, Pakistan;
    ghulamali143@gmail.com
4   Department of Chemistry, University of Azad Jammu and Kashmir, Muzaffarabad 12500, Pakistan;
    smhafeezkhan@yahoo.com
5   Department of Chemistry, University of Poonch, Rawalakot Azad Kashmir 12500, Pakistan;
    shabnamshahida01@gmail.com
6   Department of Innovative Engineering, University of Salento, Edificio La Stecca, Via per Monteroni,
    73100 Lecce, Italy; patrizia.bocchetta@unisalento.it
*   Correspondence: usmanhamid506@gmail.com (M.U.H.); yakram44@gmail.com (M.Y.A.);
    faizhaltaf@gmail.com (F.A.)

Abstract: Iron oxides are considered promising electrode materials owing to their capability of lithium storage, but their poor conductivity and large volume expansion lead to unsatisfactory cycling stability. In this paper, an inexpensive, highly effective, and facile approach to the synthesis of Fe_3O_4 nanoparticles/reduced graphene oxide composite (Fe_3O_4/RGO) is designed. The synthesized Fe_3O_4/RGO composite exhibits high reversible capability and excellent cyclic capacity as an anode material in lithium-ion batteries (LIBs). A reversible capability of 701.8 mAh/g after 50 cycles at a current density of 200 mA·g^{-1} can be maintained. The synergetic effect of unique structure and high conductivity RGO promises a well soakage of electrolyte, high structure stability, leading to an excellent electrochemical performance. It is believed that the study will provide a feasible strategy to produce transition metal oxide/carbon composite electrodes with excellent electrochemical performance for LIBs.

Keywords: Fe_3O_4; RGO; LIBs; anode material

1. Introduction

Due to the development in electric-source vehicles as well as wearable and portable electric devices, the need to enhance the operational performance of rechargeable lithium-ion batteries (LIBs) is increasing day by day [1]. In particular, the growing demand of anode materials with high reversible capacity as well as long cyclic life has increased the research interest and many papers have investigated material science and electrochemical aspects of novel materials for the above stated purpose. Among all the studied materials, TMOs (transition-metal oxides) received great attention because of their high theoretical capacity values [2–8]. In particular, Fe_3O_4 is considered a prominent candidate as Li-ion battery anode because the low cost, natural abundance, environmental friendliness, and high specific capacity. However, the use of Fe_3O_4 as LIBs anode material is responsible of low cycling capacity [9,10] due to huge voltage hysteresis during charge/discharge, large volume expansion, and low electrical conductivity during the insertion and extraction of Li-ions.

Construction of nano sized Fe_3O_4 with different morphologies and architectures are among the most prominent strategies to enhance the electrochemical performance [11–13]. Fe_3O_4 nanostructuring is among the most prominent strategies to enhance the electrochemical cycling performance of LIB anodes [11–13]. These tactics proved effective as the increase in surface area resulted in better contact between electrolyte/active materials and a shortened the diffusion length for Li-ion and caused better cycling performance. An alternative way is combining the combination of Fe_3O_4 with carbonaceous materials [14–19]. Carbonaceous materials play important roles such as suppression of nanoparticle aggregation, improvement in electrical conductivity and buffers the effect of large volume changes. Although all those efforts brought good improvements, but it is still a difficult challenge to achieve excellent rate capability as well as long cycle life.

Among the carbonaceous materials, graphene nanosheets, single atom thick, two-dimensional (2D) sheet of sp^2-bond carbon atoms, possess extraordinarily high electron conductance, thermal stability, superior mechanical properties along with very high value of specific surface area [20,21]. To increase the reversible capacity and long cycling life, researchers have prepared various nanostructured TMOs/graphene composites: TiO_2/graphene [22], Mn_3O_4/graphene [23], FeO_x/graphene [24–26], Co_3O_4/graphene [27], NiO/graphene [28], CuO/graphene [29] MoO_2/graphene, etc. [30]. In comparison with their bare carbon materials, these composites show significantly better reversible capacity, high-rate performance and improved cyclic stability, ascribed to synergetic chemical coupling effects between the graphene conductive layers and the excellent capability of TMOs to store lithium-ions. Moreover, nano sized particles, rather than their bulk materials, are employed in the most cases due to the following reasons: (1) nanomaterials can considerably shorten the lithium diffusion path length compared to their bulk counterpart [31]; (2) the nano-sized material are partially able to buffer the physical strains during the lithium insertion/extraction [32]; (3) high surface area offers a large area of contact amid electrolyte and electrode which results in improved reaction kinetics [33–35]. Nevertheless, of these advances, pulverization, cracks, and cell degradation are usually unavoidable. This mechanical degradation is explained [35,36] by the weak interaction between nano particles and graphene sheets because of weak nature of Van Der Waals forces and the restacking process of 2D graphene nanosheets because of π–π interactions, resulting in the loss of the advantages of a separated atomic layer state. Another study revealed that the tight contact through oxygen bridges in the Fe_3O_4/graphene composite has a better Li-ion storage ability than the Fe_3O_4/graphene composite with a loosen contact [37]. This suggests that the one of the most important factors governing the LIB stability is the nature of the contact at the interface graphene layers/active material, which greatly influence the electrochemical performance of the composite anode. In another report, Zhi et al. reported that Li-ion storage capacity of graphene confined tin nanosheets with a face-to-face interface contact is better if compared with spherical tin particles with point-to-point contact dispersed in the graphene matrix [38]. Thus, it is hypothesized that the anode composite material based on Fe_3O_4 nanoparticles confined between the layers of reduced graphene oxide possesses the above structural features and could be able to provide LIB higher capacity and large cycle life by Fe−O−C bond formation between layers of RGO and Fe_3O_4 nano particles.

In this study, we fabricated Fe_3O_4 nanoparticles/reduced graphene oxide (Fe_3O_4/RGO) composite through a greener and facile approach. In this design, the adequate free space in the composite allows easy electrolyte access and alleviates the volume change during cycling process. RGO with a uniform distribution of Fe_3O_4 particles is established, leading to significant improvement in the electrochemical properties. The flexibility of RGO can accommodate large volume variation and constrain Fe_3O_4 particles aggregation during the discharge/charge process. Moreover, the interconnected graphene sheets can also act as a high conductive substrate and fast ion transport path, which improve the electrical conductivity and ion transport in the anode material. The Fe_3O_4/RGO composite shows exceptional lithium storage capability, high reversible capacity, better rate performance,

and stable charge/discharge cyclability (701.8 mAh/g after 50 cycles) if compared with the previous reports on Fe_3O_4/RGO [S12–S15].

2. Materials and Methods

2.1. Materials

Iron chloride ($FeCl_3 \cdot 6H_2O$), sulfuric acid, $KMnO_4$ NaOH, H_2O_2 (3 wt.% and 30 wt.%), HCl (10 wt.%) graphite, and $NaNO_3$ (sodium nitrate) were obtained from Beijing Chemicals Company (Beijing, China). Without any further purification all chemicals were used as received.

2.2. Synthesis of Fe₃O₄/RGO Composite

GO (Graphene oxide) was synthesized according to the modified Hammer's method [21]. Firstly, a stock solution was prepared by adding NaOH (300 mg) into diethylene glycol (30 mL), heated at 130 °C under nitrogen atmosphere for 1 h. This solution cooled down to 80 °C and maintained at this temperature for further use. GO (45 mg) was added to 30 mL of diethylene glycol (DEG) under ultrasonication for 1 h, then iron chloride (180 mg) was added under vigorous stirring for 1 h. Then, under continuous nitrogen gas flow and stirring the above mixture was heated and kept at 220 °C for 0.5 h. Then, an appropriate amount of stock solution was added quickly to the reaction mixture and the temperature was maintained at 220 °C. The reaction time was fixed at 1 h to ensure the completion of reaction. Finally, ethanol was used to wash the composite Fe_3O_4/RGO several times for subsequent magnetic separation and keep in a vacuum oven at 60 °C for several hours. A detailed scheme of the synthesis process is given in Scheme 1.
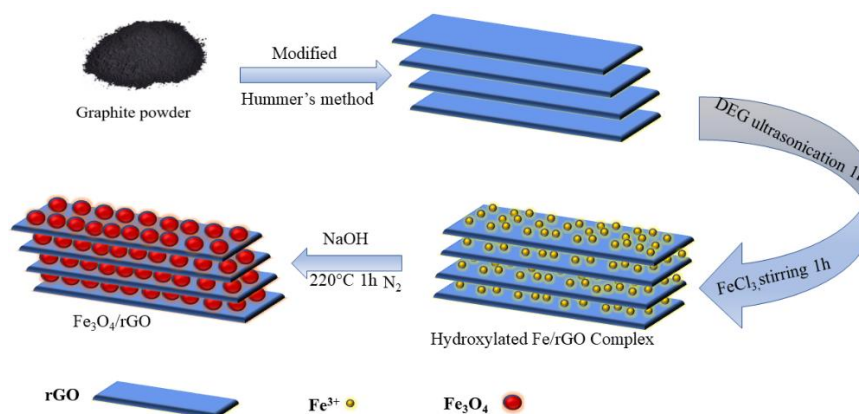
Scheme 1. Scheme of the synthesis process of Fe_3O_4/RGO composite.

2.3. Characterization

Scanning electron microscopy (JEOL JEM-6701F, Peabody, MA, USA) was utilized for surface morphological observations. X-ray diffraction (XRD: D8 system with CuKα = 1.55, motorized divergence slit with monochromator, high intensity Ka 1, 2 parallel beam, 2θ = 4°–90°, Tokyo, Japan Instrument) was employed for crystal structure analysis. TEM (transmission electron microscopy) was performed using a JEOL JEM-3010F (Peabody, MA, USA) model and XPS (X-ray photoelectron spectroscopy) using a K-Alpha Thermo Fisher Scientific, Waltham, MA, USA) to measure the atomic concentrations of composite surface and chemical binding energies. Surface area measurements are carried out by nitrogen adsorption-desorption at 77 K on a micromeritics Asap 2460 using the BET (Brunauer–Emmett–Teller) theory. To check the thermal stability of composite, thermogravimetric analysis (TA SDT Q600 instrument, New Castle, DE, USA) was performed under N_2/atm at a heating rate of 10 °C·min^{-1} from 25 to 800 °C. Degree and type of defects in the composite were determined by Raman spectroscopy (Renishaw RM1000 confocal microscope, R&R Sales and Engineering, LLC, Renishaw GmbH, Pliezhausen, Germany).

2.4. Electrochemical Measurements

The electrochemical properties of the as-synthesized composite are studied by using a coin type cell. The assembly of cell is performed in a glove box in Ar atmosphere. The as-prepared composite material was used as the working electrode materials. The slurry coating method was used for the preparation of the working electrode with a composition of 70 wt.% of composite, 20 wt.% of carbon black, and 10 wt.% ploy (vinylidene difluoride) in N- methyl pyrrolidinone. After that, the slurry was homogenously casted onto nickel foam and vacuum dried at 140 °C for 20 h. Metallic lithium foil was used as counter electrode 1 M $LiPF_6$ was used as electrolyte in a mixture of ethyl carbonate/diethyl carbonate (EC/DEC) with a volumetric ratio of 1:1. The charge/discharge profiles test were taken in the voltage range of 0.02–3.0 V at a constant current density of 200 mA/g. Ciclovoltammetry (CV) and Electrochemical Impedance Spectroscopy (EIS) measurements at the as-prepared anode material were taken using a workstation (CHI 660B). The CV measurements were employed within the range of 0.02–3.0 V at a constant rate of 0.1 mV·s^{-1}. A frequency range from 100 kHz to 10 MHz was used to perform the EIS measurements.

3. Results

XRD patterns of the prepared GO and Fe_3O_4/RGO nanocomposite are reported in Figure 1. The GO pattern shows two peaks positioned around 2θ = 10.9° and 42.6°, which are characteristic XRD diffraction peaks of GO. Introduction of different oxygen functionalities (such as epoxy carbonyl, hydroxyl) appearing at the surface of GO sheet due to strong oxidization are evidenced by the peak at 10.9° whereas the peak centered at 42.6° is characteristic of (100) plane of hexagonal structure of carbon [39,40]. The diffraction peaks shown by Fe_3O_4/RGO composite are characteristic of the magnetite face-centered cubic structure (JCPDS card No. 19-0629). An additional (002) diffraction peak around 25° in Fe_3O_4/RGO composite can be attributed to less agglomerated and disordered sheets of RGO.
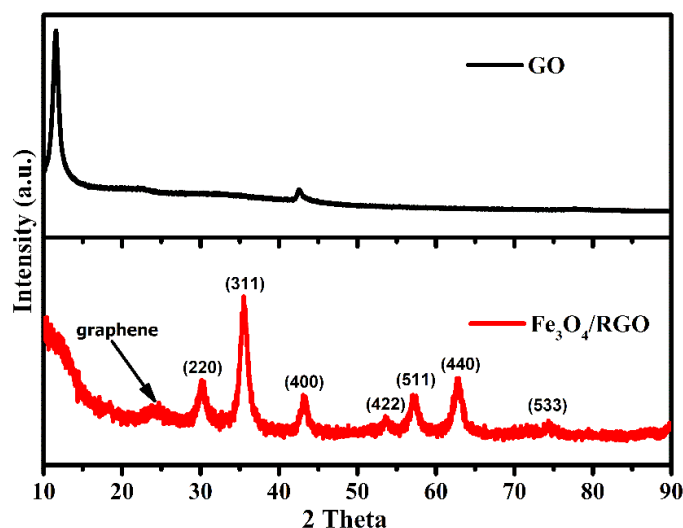
Figure 1. XRD patterns of GO and Fe_3O_4/RGO composite material.

Thermogravimetric Analysis (TGA) curves of GO and Fe_3O_4/RGO composite are shown in Figure 2a. The sample was heated under nitrogen atmosphere from 20 to 800 °C at 10 °C·min^{-1}. The initial weight loss observed from room temperature to 150 °C in the curve relating to GO is due to the evaporation of adsorbed water. Approximately at 300 °C, the substantial increase in weight loss is attributed to the removal of various oxygen containing functionalities. The subsequent decrease from 350 °C onwards to 800 °C can be ascribed to the pyrolysis of carbon skeleton as well as to the elimination of more thermal stable oxygen functionalities. In contrast, the TGA curve of Fe_3O_4/RGO

composite shows a greatly constrained weight loss. This phenomenon indicated that Fe_3O_4 NPs established in the composite a strong interaction with RGO layers. This caused a restriction effect on movement of RGO sheets which avoid heat concentration and thus helped in homogeneous heating of composite [41]. Raman spectra of GO and Fe_3O_4/RGO composite are shown in Figure 2b. Raman is a very useful technique to study the nature of pristine and composite carbon materials giving insight in the structural feathers before and after composite formation. Raman spectra of GO showed two peaks around ~1349 and ~1599 cm^{-1} characteristic of disordered carbon D band and ordered carbon G bands, respectively. The D band peak is due to the sp^3 carbon atoms of disordered graphite and the peak relating to G band can be ascribed to the in-plane vibrations of sp^2 carbon atoms. Fe_3O_4/RGO composite Raman spectrum also shows both D and G bands as prominent peaks, but the G band is slightly shifted towards lower wavenumber from ~1599–1589 cm^{-1}, giving an indication of the reduction of GO. In case of GO, D band peak is higher as compared to G band peak while in case of Fe_3O_4/RGO D band peaks is lower as compared to G band peak. The I_D/I_G ratio is another feature of the Raman spectrum, which gives useful information about the reduction of GO; in case of reduction the value of I_D/I_G ratios increases. For the Fe_3O_4/RGO composite, the I_D/I_G ratio is estimated to be 1.83 while for GO a value of 1.76 is calculated. This increase in intensity ratios indicates more defects and high degree of disorderliness (presence of localized sp^3 defects within the sp^2 carbon skeleton [42]).
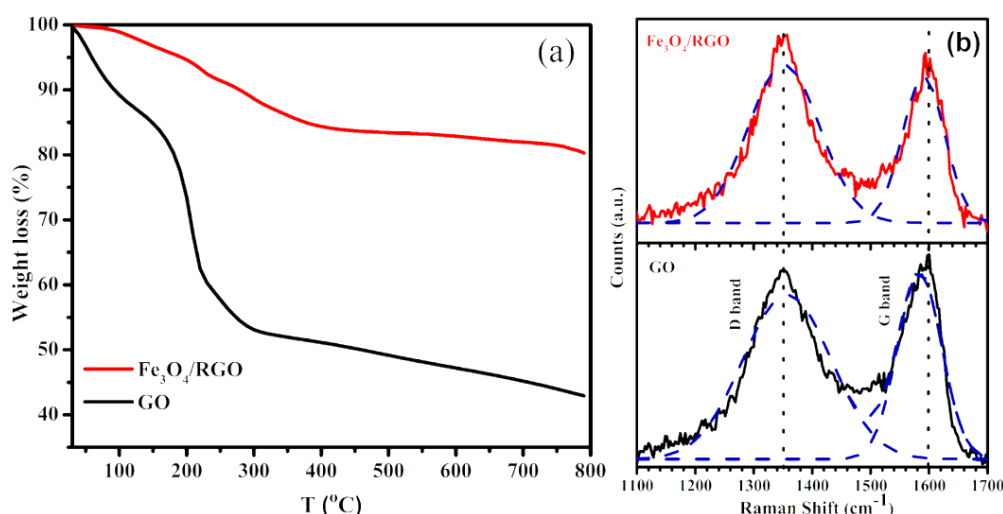
Figure 2. (**a**) TGA and (**b**) Raman analysis of GO and Fe_3O_4/RGO.

Figure 3a shows the XPS survey spectrum in the energy range of 0–1300 eV of GO and Fe_3O_4/RGO composite material. Fe, O, and C elements are detected for Fe_3O_4/RGO composite sample and C and O elements for GO sample as expected. By using XPS peak fitting software, C 1s spectra of GO could be resolved into four peaks, which were situated around 288.8, 287.8, 286.7, and 284.5 eV. In the case of GO, the atomic percentages were found to be 59.4 and 40.6 for carbon and oxygen, respectively, corresponding to an O/C atomic ratio of 0.68. C 1s spectra relating to Fe_3O_4/RGO composite shows a decrease in peak lie at 286.7 suggesting the decrease in C–O and C=O functional groups in the composite, while all the other peaks are similar to the peaks recorded in the C 1s spectra of GO. Figure 3d showed the Fe 2p high resolution XPS spectrum of Fe_3O_4/RGO composite. The peaks at 711.7 and 725.3 eV correspond to the Fe 2$p3/2$ and Fe 2$p1/2$ orbitals, respectively, in agreement with previously published values for Fe_3O_4 [43]. The absence of any peak around 720 eV confirms that no charge transfer satellite of Fe 2$p3/2$ was present, and thus the formation of mixed oxides of Fe^{+3} and Fe^{+2} can be excluded [44].
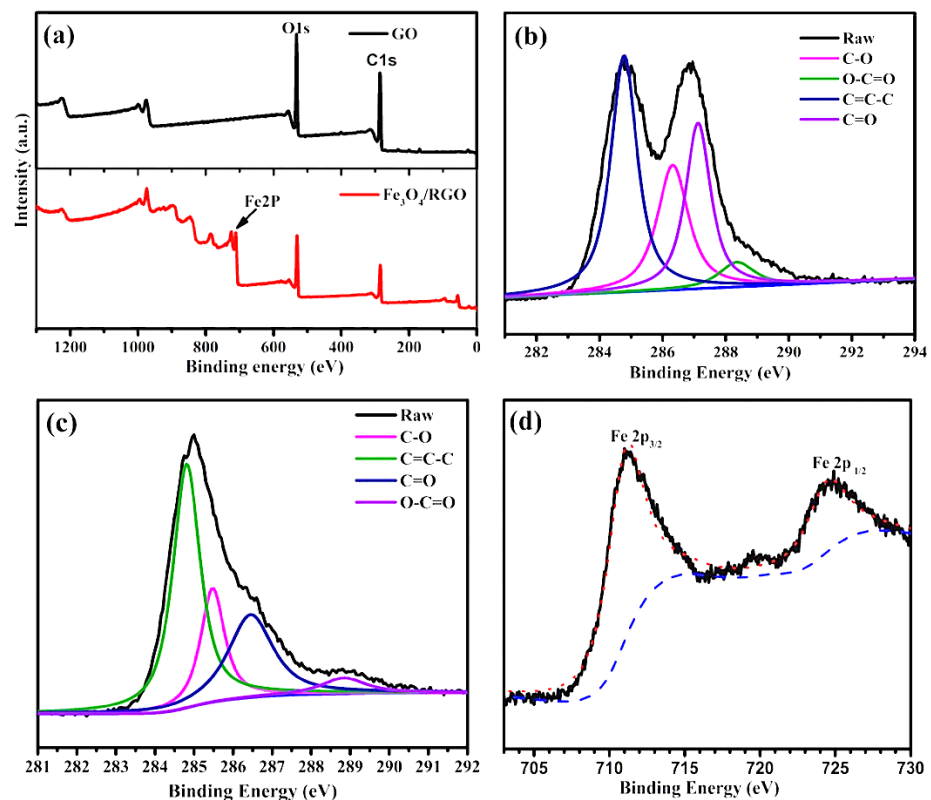
Figure 3. (**a**) XPS survey spectra of GO and Fe_3O_4/RGO, (**b**) C 1*s* region of GO, (**c**) C 1*s* region of Fe_3O_4/RGO, and (**d**) Fe 2*p* region of Fe_3O_4/RGO.

SEM analysis reported in (Figure 4a,b), shows that Fe_3O_4/RGO composite is formed by RGO individual sheets densely covered by uniform sized Fe_3O_4 NPs without any visible and significant agglomerations. These dense coverings of ultra-fine Fe_3O_4 NPs on both the sides of RGO layers not only increase thermal stability, as revealed by TGA analysis, but it is also expected to improve the conductivity of composite. The reduction of GO partially restores the π electronic system, which can cause prominent restacking of reduced graphene layers due to π-π interactions. This uniform covering of Fe_3O_4 NPs also makes difficult the restacking of reduced graphene layers of GO because reduction of GO and Fe^{3+} ions to Fe_3O_4 NPs occurs simultaneously in one step. No visible uncovered RGO is found in SEM pictures. At higher magnifications (Figure 4 c,d) one can see the sheet structure of RGO in the composite. This morphology is believed to provide an easy path for Li ions diffusion and to accommodate the volume changes effect adding up the specific capacity of the LIB. Energy-dispersive X-ray spectroscopy (EDX) element mapping was employed to estimate the iron oxide nanoparticles in the composite and the uniformity of their dispersion in the RGO substrate (Figure S1 Supplementary Information). EDX analysis revealed the excellent uniform dispersion of iron oxide nanoparticles with a Fe weight content of 23.94 wt.%. TEM images of RGO/Fe_3O_4 NPs composite are shown in Figure 4 e,f. The presence of large amounts of oxygenated functionalities, such as epoxy, carboxyl, and hydroxyl, at surface of GO sheets help to anchor hydroxylated iron complexes onto the surfaces of GO sheets. Fe_3O_4 NPs are grown on GO sheets to form surface-bound oxygen bridges nanocomposites at elevated temperature in alkaline media with the addition of NaOH. Figure 4e,f shows the tight bond between the components in agreement with TGA and XPS results. TEM also revealed that individual RGO sheets are densely and homogeneously covered with Fe_3O_4 NPs of uniform diameter. TEM images (e,f) further support the SEM findings. No obvious uncovered portions as well as no considerable odd size particles can be found.
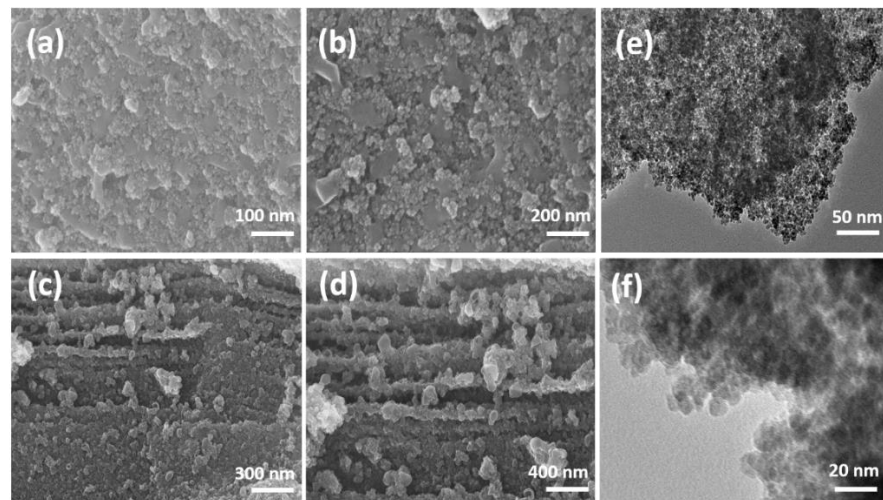
Figure 4. (**a–d**) SEM and (**e,f**) TEM images at different magnifications of Fe_3O_4/RGO composite.

N_2 absorption/desorption isotherm has been carried out to measure the surface area and porosity of as prepared composite and reported in Figure 5a,b. The surface area of the composite is measured by BET as 103.29 m^2/g. The value is quite high and gives an indication about the presence of active and functional sites. The Barrett, Joyner, and Halenda desorption gives a pore volume of 0.209235 cm^3/g. Highly dispersed RGO contributes to the high value of surface area of the Fe_3O_4/RGO composite, which in turn offer easy diffusion of the electrolyte and a large number of active sites [45]. The hysteretic curve of Fe_3O_4/RGO is a type "IV" isotherm characteristic of mesoporous materials. The high surface area can make easy and rapid insertion/extraction of Li^+ ions because of presence of additional channels and active sites in composite anode material. The sheet structure of the composite not only buffers the volume changes during charging/discharging steps, but also assists diffusion of solid-state Li^+ ions to maintain the overall integrity of the structure. PSD curves shows a maximum distribution of the pores between 0.5 to 6 nm.
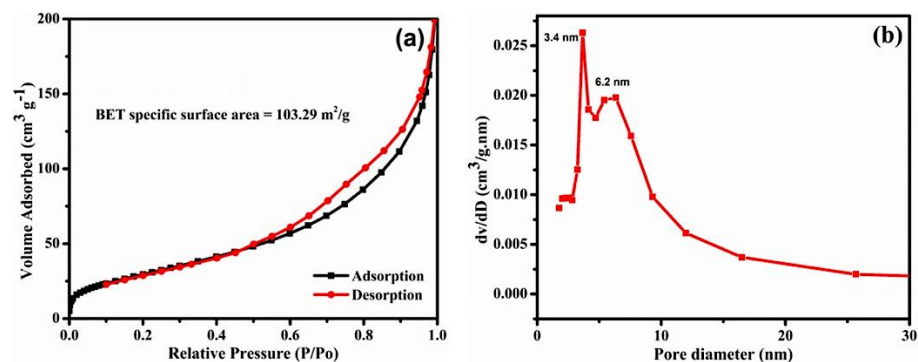
Figure 5. (**a**) Nitrogen adsorption-desorption isotherms and (**b**) PSD of Fe_3O_4/RGO composite.

Electrochemical Properties

Figure 6a displays the charge/discharge profiles of as-synthesized Fe_3O_4/RGO composite anode for the first three cycles at a current density of 200 mA/g within the voltage range of 0.02–3.0 V.
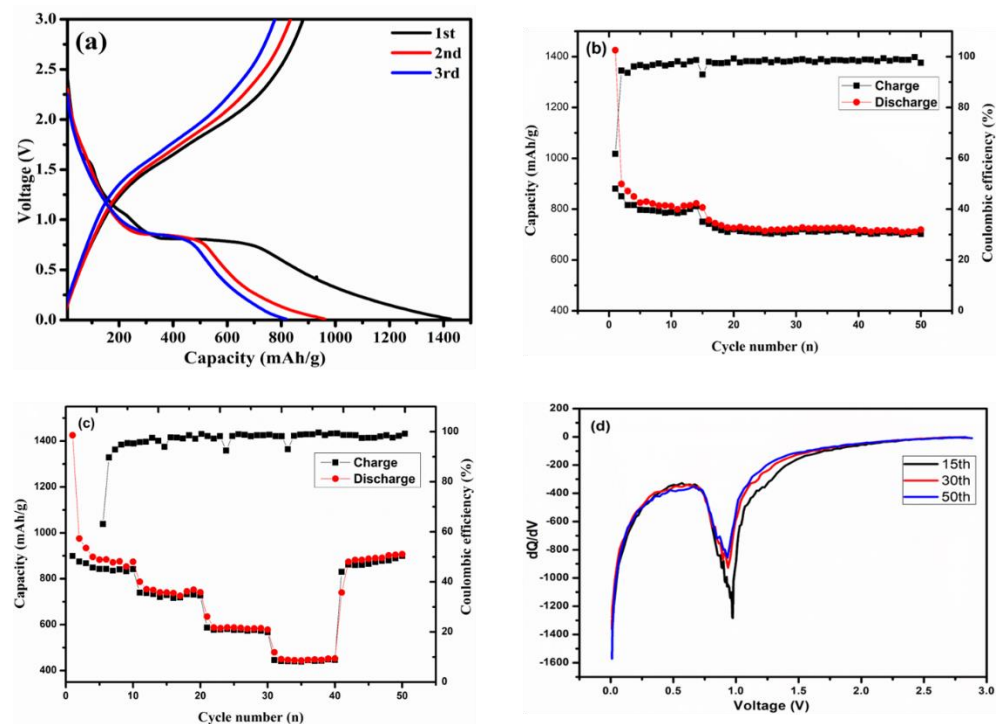
Figure 6. (**a**) Discharge–charge curves of RGO/Fe$_3$O$_4$ at a current density of 200 mA/g; (**b**) cycling performance of Fe$_3$O$_4$/RGO at a current density of 200 mA/g; (**c**) rate capacities of Fe$_3$O$_4$/RGO at 200–1500 mA/g; (**d**) differential plots of capacity vs. cell voltage.

The discharge/charge capacities are initially 1425.7 and 880.8 mAh/g, respectively. The capacity loss observed at the first cycle for most of the samples is about 62% due to the irreversible Solid Electrolyte Interphase (SEI) formation. During the first discharge step, at about 0.8 V a long voltage plateau tailed by a sloping curve down to the cut voltage of 0.01 V was observed for all the recorded curves. This behavior depends on the features of voltage drifts characteristic of the Fe$_3$O$_4$ electrode [46,47]. It is well-known that the sheet type structure of Fe$_3$O$_4$/RGO may trap more lithium ions during electrochemical cycling, which resulted in large irreversible capacities. The reversibility of the composite electrode is significantly improved in the 2nd cycle. After the 3rd cycle, the discharge/charge capacities are 871.3 and 816 mAh/g, respectively, and the columbic efficiency exceeds 94% signifying a better capacity retention of the electrode. The slight capacity change in the successive cycles is attributed to the maximum probability of finding favorable sites for Li$^+$ ion migration in the nanoscaled Fe$_3$O$_4$ particles. Consequently, the increase in reversible capacities could be ascribed to the fast lithium ion and transport of electron through covalent interaction between the Fe$_3$O$_4$ nanoparticles and RGO. Moreover, the Fe$_3$O$_4$ NPs can enable the infiltration of electrolyte which is responsible to speed up the lithium-ion transport.

Figure 6b shows the cyclic performance of as-synthesized Fe$_3$O$_4$/RGO composite. Fe$_3$O$_4$/RGO nanocomposite electrodes exhibit better reversible capacity at a current density of 200 mA/g after 50 cycles. The retentive capacity (701.8 mAh/g) after 50 cycles is 83% of the second reversible charge capacity (850.1 mAh/g) indicating the longer cycling life and excellent strength of the electrode. Throughout successive electrochemical cycling (at about the 15th cycle) a fading of capacity is observed in all samples and attributed to the mechanical damage/severe fracture or to the agglomeration of Fe$_3$O$_4$ NPs owing to the drastic volume changes along with the conversion reaction. Nevertheless, the Fe$_3$O$_4$/RGO composite investigated in this work show better rate performance and stable charge/discharge cyclability (701.8 mAh/g after 50 cycles) if compared with the previous reports on Fe$_3$O$_4$/RGO and similar Fe-containing composites. A comprehensive

comparison between the electrochemical performances of the Fe_3O_4/RGO composites studied in this paper and the Fe_3O_4/graphene and Fe_3O_4/carbon materials previously reported in literature is shown in Table S1 and references therein (Supporting information). This improvement is attributed to the homogenous decoration of Fe_3O_4 NPs in the layered graphene observed in the Fe_3O_4/RGO composite electrode by SEM and TEM analysis and confirmed by TGA measurements. Such a dimensional confinement of the Fe_3O_4 NPs by the surrounding graphene layers reduces the volume increase effect upon insertion of lithium. As a consequence, graphene layers provide a conductive network favorable to the electron transfer during lithiation/delithiation process.

The electrode rate capabilities were also evaluated at various current densities as depicted in Figure 6c. The differential plots of capacity vs. cell voltage presents in Figure 6d shows the lithium storage capability of Fe_3O_4/RGO is mainly at the voltage of capacity 0.5 V.

As the current density increases from 200 to 1500 mA/g, the decrease in discharge capacity is attributed to the controlled-diffusion kinetics process for the electrode reaction. After 10 cycles the discharge capacity noted for Fe_3O_4/RGO composite is 874.1 mAh/g at a current density of 200 mA/g. The discharge capacities of Fe_3O_4/RGO still remain at 740.8, 578.1, and 452.4 mAh/g even at a very high current density of 500, 1000, and 1500 mA/g, respectively. Furthermore, an excellent reversibility was obtained after deep cycling at 1500 mA/g; when the current density brings back to 200 mA/g, the discharge capacity still retains at 875.3 mAh/g. According to our knowledge, the Fe_3O_4/RGO composite synthesized by using the method described in this paper possess an improved rate retention property if used as anode in an LIB. A comparison between carbon-based Fe_3O_4 composite anodes for LIBs reported in previous studies is given in Table S1 (supplementary information). Structure stability and high electrochemical activity is answerable for the improved electrochemical performance of the composite material.

The reversible reaction of Li ions with as synthesized Fe_3O_4/RGO composite was explored in view of practical application as anode material in Li-ion batteries. Figure 7 shows the CV curves (first three cycles) of Fe_3O_4/RGO composite electrode at a scan rate of 0.1 mV·s^{-1}.
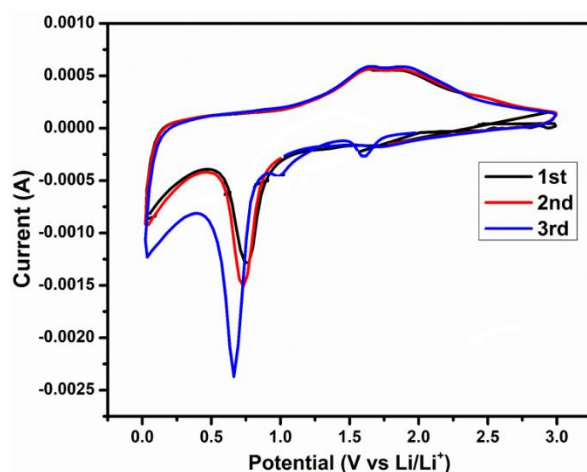
Figure 7. Cyclic Voltammograms of the Fe_3O_4/RGO composite electrode at a scan rate of 0.1 mV/s.

During the first cathodic scan of Fe_3O_4/RGO composite, the sharp reduction peak observed at about 0.7 V is ascribed to the irreversible reaction with electrolyte and to the reduction to the different oxidation states of iron (Fe^{3+} or Fe^{2+} to Fe^0) [17]. Furthermore, the two reduction peaks of less intensity at 0.9 and 1.5 V can be attributed to the formation of $Li_xFe_3O_4$ [48,49]. During the first discharge potential scan, the conversion of Fe_3O_4 to Fe and formation of Li_2O could be the key reason for irreversible capacity.

In the meantime, the reversible oxidation of Fe^0 to Fe^{2+}/Fe^{3+} is evidenced by the two anodic peaks at 1.63 and 1.85 V [46]. The shift of the redox peaks in succeeding cycles occurs owing to structural modifications. It is worth noting that the area underlying the peak at 1.85 V is larger for second and third cycle accounting for the reversible reaction of Fe_3O_4. Moreover, after the first cycle no obvious changes were found in peak intensity as well as in integrated area of both anodic and cathodic peaks, signifying that the electrochemical reversibility of Fe_3O_4-graphene become stable after the initial cycle. The CV results are in good agreement with the charge/discharge results.

To further verify the improved electrochemical properties of the as-synthesized composite, EIS measurements were employed. The Nyquist plot of Fe_3O_4/RGO composite after five cycles at a current density of 200 mA/g are shown in Figure 8. From the plot it can be qualitatively observed that the diameter of the semicircle relating to the Fe_3O_4/RGO composite is small (24 Ω) indicating that the Fe_3O_4/RGO composite electrode considerably lowers the contact and charge transfer resistances thanks to the high content of carbon and layered structure of graphene [50].
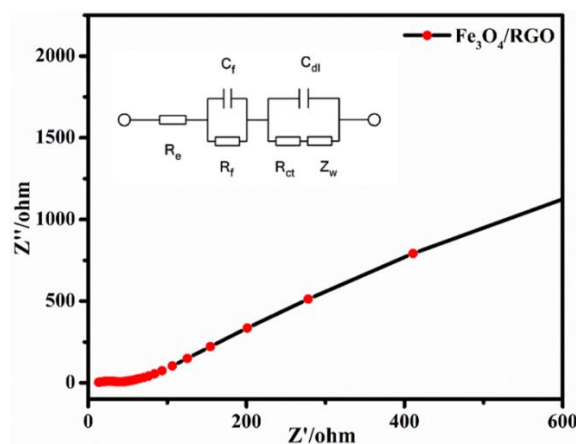
Figure 8. Nyquist plot relating to Fe_3O_4/RGO composite electrode after 5 cycles at a current density (200 mA/g). Inset: equivalent circuit used to discuss the data. R_e: electrolyte resistance, R_{ct}: charge transfer resistance, C_{dl}: double layer capacitance, Z_w: Warburg element.

This result corroborates with XPS, TGA and Raman results indicating that a strong contact between Fe_3O_4 and RGO sheets can effectively increase the charge transfer and reduce the contact resistances.

4. Conclusions

A simple and facile approach was developed to obtain Fe_3O_4/RGO composite in which Fe_3O_4 NPs homogenously cover the surface of RGO sheets. The improved electrochemical performance was attributed to the synergistic effect between Fe_3O_4 NPs and RGO. The Fe_3O_4/RGO composite exhibited an outstanding specific capacity up to 701.8 mAh/g after 50 cycles, even at a high current density of 1500 mA/g. The composite possesses considerable higher capacity (446.4 mAh/g) owing to the sheet structural symmetry. The graphene sheets can effectively reduce the lithium diffusion paths offering better conductivity, as well as provide large contact area for the Fe_3O_4 NPs. The results discussed in this paper allow to conclude that the Fe_3O_4/RGO composite represents a promising anode material for LIBs.

References

1.　Zheng, G.; Lee, S.W.; Liang, Z.; Lee, H.W.; Yan, K.; Yao, H.; Wang, H.; Li, W.; Chu, S.; Cui, Y. Interconnected Hollow Carbon Nanospheres for Stable Lithium Metal Anodes. *Nat. Nanotechnol.* **2014**, *9*, 618–623. [CrossRef]

2.　Lü, H.Y.; Wan, F.; Jiang, L.H.; Wang, G.; Wu, X.L. Graphene Nanosheets Suppress the Growth of Sb Nanoparticles in a Sb/C Nanocomposite to Achieve Fast Na Storage. *Part. Part. Syst. Charact.* **2016**, *33*, 204–211. [CrossRef]

3.　Hou, B.H.; Wu, X.L.; Wang, Y.Y.; Lü, H.Y.; Liu, D.H.; Sun, H.Z.; Zhang, J.P.; Guan, H.Y. Full Protection for Graphene- Incorporated Micro-/Nanocomposites Containing Ultra-Small Active Nanoparticles: The Best Li-Storage Properties. *Part. Part. Syst. Charact.* **2015**, *32*, 1020–1027. [CrossRef]

4.　Guo, J.Z.; Wu, X.L.; Wan, F.; Wang, J.; Zhang, X.; Wang, H.R.S. A Superior $Na_3V_2(PO_4)_3$ Based Nanocomposite Enhanced by Both N-Doped Coating Carbon and Graphene as the Cathode for Sodium-Ion Batteries. *Chem. Eur. J.* **2015**, *21*, 17371–17378. [CrossRef]

5.　Liu, D.H.; Lü, H.Y.; Wu, X.L.; Hou, B.H.; Wan, F.; Bao, S.D.; Yan, Q.Y.; Xie, H.M.; Wang, R.S. Constructing the Optimal Conductive Network in MnO-Based Nanohybrids as High-Rate and Long-Life Anode Materials for Lithium-Ion Batteries. *J. Mater. Chem. A* **2015**, *3*, 19738–19746. [CrossRef]

6.　Wang, J.; Liu, D.H.; Wang, Y.Y.; Hou, B.H.; Zhang, J.P.; Wang, R.S.; Wu, X.L. Dual-Carbon Enhanced Silicon-Based Composite as Superior Anode Material for Lithium Ion Batteries. *J. Power Sources* **2016**, *307*, 738–745. [CrossRef]

7.　Kumar, R.; Singh, R.K.; Dubey, P.K.; Singh, D.P.; Yadav, R.M.; Tiwari, R.S. Free standing 3D Graphene-Nickel Encapsulated Nitrogen-Rich Aligned Bamboo Like Carbon Nanotubes for High- Performance Supercapacitors with Robust Cycle Stability. *Adv. Mater. Interfaces* **2015**, *2*, 1–12. [CrossRef]

8.　Kumar, R.; Singh, R.K.; Dubey, P.K.; Singh, D.P.; Yadav, R.M. Self-Assembled Hierarchical Formation of Conjugated 3D Cobalt Oxide Nanobead-CNT-Graphene Nanostructure Using Microwaves for High-Performance Supercapacitor Electrode. *ACS Appl. Mater. Interfaces* **2015**, *7*, 15042–15051. [CrossRef] [PubMed]

9.　Dong, Y.C.; Ma, R.G.; Hu, M.J.; Cheng, H.; Tsang, C.K.; Yang, Q.D.; Li, Y.Y.; Zapien, J.A. Scalable Synthesis of Fe_3O_4 Nanoparticles Anchored on Graphene as a High-Performance Anode for Lithium Ion Batteries. *J. Solid State Chem.* **2013**, *201*, 330–337. [CrossRef]

10.　Liu, S.Y.; Xie, J.; Fang, C.C.; Cao, G.S.; Zhu, T.J.; Zhao, X.B. Self-Assembly of a $CoFe_2O_4$/Graphene Sandwich by a Controllable and General Route: Towards a High-Performance Anode for Li-Ion Batteries. *J. Mater. Chem.* **2012**, *37*, 19738–19743. [CrossRef]

11.　Dong, Y.C.; Ma, R.G.; Hu, M.J.; Cheng, H.; Yang, Q.D.; Li, Y.Y.; Zapien, J.A. Thermal Evaporation-Induced Anhydrous Synthesis of Fe_3O_4–Graphene Composite with Enhanced Rate Performance and Cyclic Stability for Lithium Ion Batteries. *Phys. Chem. Chem. Phys.* **2013**, *15*, 7174–7181. [CrossRef] [PubMed]

12.　Behera, S.K. Facile Synthesis and Electrochemical Properties of Fe_3O_4 Nanoparticles for Li Ion Battery Anode. *J. Power Sources* **2011**, *196*, 8669–8674. [CrossRef]

13.　Chen, Y.; Xia, H.; Lu, L.; Xue, J.M. Synthesis of Porous Hollow Fe_3O_4 Beads and Their Applications in Lithium Ion Batteries. *J. Mater. Chem.* **2012**, *22*, 5006–5012. [CrossRef]

14.　Kang, E.; Jung, Y.S.; Cavanagh, A.S.; Kim, G.H.; George, S.M.; Dillon, A.C.; Kim, J.K.; Lee, J. Fe_3O_4 Nanoparticles Confined in Mesocellular Carbon Foam for High Performance Anode Materials for Lithium-Ion Batteries. *Adv. Funct. Mater.* **2011**, *21*, 2430–2438. [CrossRef]

15.　Ban, C.M.; Wu, Z.C.; Gillaspie, D.T.; Chen, L.; Yan, Y.F.; Blackburn, J.L.; Dillon, A.C. Nanostructured Fe_3O_4/SWNT Electrode: Binder-Free and High-Rate Li-Ion Anode. *Adv. Mater.* **2010**, *22*, E145–E149. [CrossRef]

16.　Liu, H.; Wang, G.X.; Wang, J.Z.; Wexler, D. Magnetite/Carbon Core-Shell Nanorods as Anode Materials for Lithium-Ion Batteries. *Electrochem. Commun.* **2008**, *10*, 1879–1882. [CrossRef]

17.　Xiong, Q.Q.; Tu, J.P.; Lu, Y.; Chen, J.; Yu, Y.X.; Qiao, Y.Q.; Wang, X.L.; Gu, C.D. Synthesis of Hierarchical Hollow-Structured Single-Crystalline Magnetite (Fe_3O_4) Microspheres: The Highly Powerful Storage versus Lithium as an Anode for Lithium Ion Batteries. *J. Phys. Chem. C* **2012**, *116*, 6495–6502. [CrossRef]

18.　Chen, Y.J.; Xiao, G.; Wang, T.S.; Ouyang, Q.Y.; Qi, L.H.; Ma, Y.P.; Gao, C.L.; Zhu, M.S.; Cao, M.S.; Jin, H.B. Porous Fe_3O_4/Carbon Core/Shell Nanorods: Synthesis and Electromagnetic Properties. *J. Phys. Chem. C* **2011**, *115*, 13603–13608. [CrossRef]

19. Xiong, Q.Q.; Tu, J.P.; Lu, Y.; Chen, J.; Yu, Y.X.; Wang, X.L.; Gu, C.D. Three-Dimensional Porous Nano-Ni/Fe$_3$O$_4$ Composite Film: Enhanced Electrochemical Performance for Lithium-Ion Batteries. *J. Mater. Chem.* **2012**, *22*, 18639–18645. [CrossRef]

20. Balandin, A.A.; Ghosh, S.; Bao, W.Z.; Calizo, I.; Teweldebrhan, D.; Miao, F.; Lau, C.N. Superior Thermal Conductivity of Single-Layer Graphene. *Nano Lett.* **2008**, *8*, 902–907. [CrossRef]

21. Yoo, E.J.; Kim, J.; Hosono, E.; Zhou, H.S.; Kudo, T.; Honma, I. Large Reversible Li Storage of Graphene Nanosheet Families for Use in Rechargeable Lithium Ion Batteries. *Nano Lett.* **2008**, *8*, 2277–2282. [CrossRef]

22. Wang, D.H.; Choi, D.W.; Li, J.; Yang, Z.G.; Nie, Z.M.; Kou, R.; Hu, D.H.; Wang, C.M.; Saraf, L.V.; Zhang, J.G.; et al. Self-Assembled TiO$_2$-Graphene Hybrid Nanostructures for Enhanced Li-Ion Insertion. *ACS Nano* **2009**, *3*, 907–914. [CrossRef]

23. Wang, H.L.; Cui, L.F.; Yang, Y.; Casalongue, H.S.; Robinson, J.T.; Liang, Y.Y.; Cui, Y.; Dai, H.J. Mn$_3$O$_4$-Graphene Hybrid as a High-Capacity Anode Material for Lithium Ion Batteries. *J. Am. Chem. Soc.* **2010**, *132*, 13978–13980. [CrossRef] [PubMed]

24. Su, J.; Cao, M.H.; Ren, L.; Hu, C.W. Fe3O4-Graphene Nanocomposites with Improved Lithium Storage and Magnetism Properties. *J. Phys. Chem. C* **2011**, *115*, 14469–14477. [CrossRef]

25. Lian, P.C.; Zhu, X.F.; Xiang, H.F.; Li, Z.; Yang, W.S.; Wang, H.H. Enhanced Cycling Performance of Fe$_3$O$_4$-Graphene Nanocomposite as an Anode Material for Lithium-ion Batteries. *Electrochim. Acta* **2010**, *56*, 834–840. [CrossRef]

26. Zhou, G.M.; Wang, D.W.; Li, F.; Zhang, L.L.; Li, N.; Wu, Z.S.; Wen, L.; Lu, G.Q.; Cheng, H.M. Graphene-Wrapped Fe$_3$O$_4$ Anode Material with Improved Reversible Capacity and Cyclic Stability for Lithium Ion Batteries. *Chem. Mater.* **2010**, *22*, 5306–5313. [CrossRef]

27. Li, B.J.; Cao, H.Q.; Shao, J.; Li, G.Q.; Qu, M.Z.; Yin, G. Co$_3$O$_4$@graphene Composites as Anode Materials for High-Performance Lithium Ion Batteries. *Inorg. Chem.* **2011**, *50*, 1628–1632. [CrossRef] [PubMed]

28. Zou, Y.Q.; Wang, Y. NiO Nanosheets Grown on Graphene Nanosheets as Superior Anode Materials for Li-Ion Batteries. *Nanoscale* **2011**, *3*, 2615–2620. [CrossRef] [PubMed]

29. Wang, B.; Wu, X.L.; Shu, C.Y.; Guo, Y.G.; Wang, C.R. Synthesis of CuO/Graphene Nanocomposite as a High-Performance Anode Material for Lithium-Ion Batteries. *J. Mater. Chem.* **2010**, *20*, 10661–10664. [CrossRef]

30. Sun, Y.M.; Hu, X.H.; Luo, W.; Huang, Y.H. Self-Assembled Hierarchical MoO$_2$/Graphene Nanoarchitectures and Their Application as a High-Performance Anode Material for Lithium-Ion Batteries. *ACS Nano* **2011**, *5*, 7100–7107. [CrossRef] [PubMed]

31. Wang, Y.; Zhang, H.J.; Lu, L.; Stubbs, L.P.; Wong, C.C.; Lin, J.Y. Designed Functional Systems from Peapod-like Co@Carbon to Co$_3$O$_4$@Carbon Nanocomposites. *ACS Nano* **2010**, *4*, 4753–4761. [CrossRef]

32. Guo, Y.G.; Hu, J.S.; Wan, L.J. Nanostructured Materials for Electrochemical Energy Conversion and Storage Devices. *Adv. Mater.* **2008**, *20*, 2878–2887. [CrossRef]

33. Bruce, P.G.; Scrosati, B.; Tarascon, J.-M. Nanomaterials for Rechargeable Lithium Batteries. *Angew. Chem. Int. Ed.* **2008**, *47*, 2930–2946. [CrossRef]

34. Chen, Y.; Song, B.H.; Li, M.; Lu, L.; Xue, J.M. Fe$_3$O$_4$ Nanoparticles Embedded in Uniform Mesoporous Carbon Spheres for Superior High-Rate Battery Applications. *Adv. Funct. Mater.* **2014**, *24*, 319–326. [CrossRef]

35. Sun, Y.M.; Hu, X.L.; Luo, W.; Huang, Y.H. Ultrathin CoO/ Graphene Hybrid Nanosheets: A Highly Stable Anode Material for Lithium-Ion Batteries. *J. Phys. Chem. C* **2012**, *116*, 20794–20799. [CrossRef]

36. Gong, Y.J.; Yang, S.B.; Zhan, L.; Ma, L.L.; Vajtai, R.; Ajayan, P.M. A Bottom-Up Approach to Build 3D Architectures from Nanosheets for Superior Lithium Storage. *Adv. Funct. Mater.* **2014**, *24*, 125–130. [CrossRef]

37. Zhou, J.; Song, H.; Ma, L.; Chen, X. Magnetite/Graphene Nanosheet Composites: Interfacial Interaction and its Impact on the Durable High-Rate Performance in Lithium-Ion Batteries. *RSC Adv.* **2011**, *1*, 782–791. [CrossRef]

38. Luo, B.; Wang, B.; Li, X.; Jia, Y.; Liang, M.; Zhi, L. Graphene-Confined Sn Nanosheets with Enhanced Lithium Storage Capability. *Adv. Mater.* **2012**, *24*, 3538–3543. [CrossRef]

39. Chen, Q.W.; Zhang, L.Y.; Chen, G. Facile Preparation of Graphene-Copper Nanoparticle Composite by in situ Chemical Reduction for Electrochemical Sensing of Carbohydrates. *Anal. Chem.* **2012**, *84*, 171–178. [CrossRef]

40. Zhang, F.; Li, Y.; Gu, Y.-e.; Wang, Z.; Wang, C. One-Pot Solvothermal Synthesis of a Cu$_2$O/Graphene Nanocomposite and its Application in an Electrochemical Sensor for Dopamine. *Microchim. Acta* **2011**, *173*, 103–109. [CrossRef]

41. Tuinstra, F.; Koenig, J.L. Raman Spectrum of Graphite. *J. Chem. Phys.* **1970**, *53*, 1126–1130. [CrossRef]

42. Shen, J.; Shi, M.; Ma, H.; Yan, B.; Li, N.; Ye, M. Hydrothermal Synthesis of Magnetic Reduced Graphene Oxide Sheets. *Mater. Res. Bull.* **2011**, *46*, 2077–2083. [CrossRef]

43. Teng, X.W.; Black, D.; Watkins, N.J.; Gao, Y.L.; Yang, H. Platinum-Maghemite Core−Shell Nanoparticles Using a Sequential Synthesis. *Nano Lett.* **2003**, *3*, 261–264. [CrossRef]

44. Morel, A.L.; Nikitenko, S.I.; Gionnet, K.; Wattiaux, A.; Lai-Kee-Him, J.; Labrugere, C.; Chevalier, B.; Deleris, G.; Petibois, C.; Brisson, A.; et al. Sonochemical Approach to the Synthesis of Fe$_3$O$_4$@SiO$_2$ Core−Shell Nanoparticles with Tunable Properties. *ACS Nano* **2008**, *2*, 847–856. [CrossRef] [PubMed]

45. Yin, X.; Wu, S.; Dastan, D.; Nie, S.; Liu, Y.; Li, Z.; Zhou, Y.; Li, J.; Faik, A.; Shan, K.; et al. Sensing Selectivity of SnO$_2$-Mn$_3$O$_4$ Nanocomposite Sensors for the Detection of H$_2$ and CO Gases. *Surf. Interfaces* **2021**, *25*, 101190. [CrossRef]

46. He, Y.; Huang, L.; Cai, J.S.; Zheng, X.M.; Sun, S.G. Structure and Electrochemical Performance of Nanostructured Fe$_3$O$_4$/Carbon Nanotube Composites as Anodes for Lithium Ion Batteries. *Electrochim. Acta* **2010**, *55*, 1140–1144. [CrossRef]

47. Poizot, P.; Laruelle, S.; Grugeon, S.; Dupont, L.; Tarascon, J.M. Nano-Sized Transition-Metal Oxides as Negative-Electrode Material for Lithium Ion Batteries. *Nature* **2000**, *407*, 496–499. [CrossRef]

48. Shan, K.; Yi, Z.Z.; Yin, X.T.; Dastan, D.; Altaf, F.; Garmestani, H.; Alamgir, F.M. Mixed Conductivity Evaluation and Sensing Characteristics of Limiting Current Oxygen Sensors. *Surf. Interfaces* **2020**, *21*, 100762. [CrossRef]
49. Yin, X.T.; Li, J.; Dastan, D.; Zhou, W.D.; Garmestani, H.; Alamgir, F.M. Ultra-High Selectivity of H_2 over CO with a p-n Nanojunction Based Gas Sensors and its Mechanism. *Sens. Actuators B Chem.* **2020**, *319*, 128330. [CrossRef]
50. Xiang, J.Y.; Tu, J.P.; Qiao, Y.Q.; Wang, X.L.; Zhong, J.; Zhang, D.; Gu, C.D. Electrochemical Impedance Analysis of a Hierarchical CuO Electrode Composed of self-Assembled Nanoplates. *J. Phys. Chem. C* **2011**, *115*, 2505–2513. [CrossRef]